# Generation of ion acoustic solitary waves through wave breaking in superthermal plasmas

Ajay Lotekar,[a] Amar Kakad,[b] and Bharati Kakad[c]
*Indian Institute of Geomagnetism, New Panvel, Navi Mumbai 410-218, India*

(Received 21 June 2017; accepted 28 September 2017; published online 23 October 2017)

Space plasmas provide abundant evidence of a highly energetic particle population that results in a long-tailed non-Maxwellian distribution. Such plasmas can be effectively modeled with kappa distribution. The superthermal population in the tail of kappa distribution can have significant effects on the wave dynamical processes. We perform the fluid simulations to examine the effects of superthermal populations on the breaking of the electrostatic ion-acoustic (IA) wave, which is the most fundamental mode, existing in the unmagnetized plasmas. We construct a fluid model for exciting IA waves by employing a kappa distribution function for the superthermal population of electrons along with inertial cold ions (protons). We focused on the nonlinear excitations; in the form of ion acoustic solitary wave (IASW) structures formed through the process of wave breaking, and investigated the role of superthermal electron population in the initiation of the steepening, wave breaking, and propagation characteristics of the IASWs in plasma. From the output of the simulation, we established the criteria for the steepening time based on the variations in the phase velocity of the IASWs. Furthermore, we examined the maximum ponderomotive potential and ponderomotive frequency during the wave breaking process. We found that the time corresponding to the peak in the maximum ponderomotive potential is the time of the initialization of the wave breaking process. We present a detailed investigation of the role of the ponderomotive forces acting on the plasma at each time step, which explains the physics of the wave breaking in nonthermal plasmas. *Published by AIP Publishing.* https://doi.org/10.1063/1.4991467

## I. INTRODUCTION

One of the most obvious features of the plasma in the Earth's or any other planetary magnetospheres is the existence of the rich variety of waves in it. The wave modes depend upon the plasma properties, which makes their study in plasma very important. The nonlinear propagation of these waves in plasma has a fundamental limitation given by the wave breaking threshold. The study of breaking of large amplitude plasma waves in plasma is a subject of both fundamental as well as practical interest as it is one of the important mechanisms for heating and acceleration of the plasma. In many practical situations like, in particle accelerator experiments, wave breaking limits the maximum achievable accelerating electric field. In this situation, a pertinent issue is the maximum magnitude of the wave electric field that can be attained without wave breaking. Wave breaking analysis goes back to classical papers by Dawson,[1] and Davidson and Schram.[2] Waves in a uniform plasma were found to be stable below the critical amplitude. For a larger amplitude, it was shown that the elements of the plasma electron fluid that started out in different positions overtake each other while moving back and forth during the passage of the wave. For non-relativistic plasmas, this overtaking happens when the peak fluid velocity equals the phase velocity of the plasma wave. Most of this wave breaking models use the fluid approach, which in electrons and ions are treated as a fluid[3,4] or one of them is considered as Maxwellian distributed. However, the plasma generally follows non-Maxwellian type distributions in the regions of space where plasma acceleration is prominent.

The nonthermal particle distributions are ubiquitous in various space plasmas, and their presence being widely confirmed by spacecraft measurements in planetary magnetospheres (e.g., plasma sheet,[5–7] magnetosheath,[8] radiation belt,[9,10] solar wind[11,12]), and laboratory[13,14] plasma. Such plasma supports the existence of highly energetic particles (electrons, in principle) at velocities exceeding the thermal speed. The presence of this excess superthermal component, which may be due to various acceleration mechanisms, gives rise to a long-tailed velocity distribution, which deviates, substantially from the Maxwellian. One approach to demonstrate the non-Maxwellian plasma is provided by the kappa distribution,[15–19] which was introduced by Vasyliunas[16] to fit phenomenologically the power law-like dependence of electron velocity distribution functions observed in space. Such distributions have high-energy tails deviated from a Maxwellian, which can incorporate the superthermal population. The three-dimensional isotropic kappa velocity distribution function has the following form:[16,17,20]

$$f_\kappa(v_s) = \frac{n_{0s}}{(\pi\kappa\theta_s^2)^{3/2}} \frac{\Gamma(\kappa+1)}{\Gamma(\kappa-1/2)} \left[1 + \frac{v_s^2}{\kappa\theta^2}\right]^{-(\kappa+1)}. \quad (1)$$

In the equation above, $\Gamma$ is the gamma function, and $n_{0s}$ and $v_s$ are the density and velocity of plasma species $s$. $\theta_s^2 = [(\kappa - 3/2)/\kappa]v_{th,s}^2$ is the most probable speed or characteristic

[a]ablotekar@gmail.com
[b]amar@iigs.iigm.res.in
[c]ebharati@iigs.iigm.res.in

speed, where $v_{th,s} = (2k_BT_s/m_s)^{1/2}$ is the thermal speed of the plasma species, $k_B$ is the Boltzmann constant. $T_s$ and $m_s$ are the temperature and mass of the plasma species. The spectral index $\kappa$ decides slope of the tail of the distribution function, and it is always greater than 1.5. The smaller value of $\kappa$ enhances the superthermal population in the system, which leads to a decrease in the slope of the tail. As the kappa index $\kappa \to \infty$, the kappa distribution function converges to the Maxwellian distribution function. For space plasma, the kappa index is observed in the range,[20] $2 < \kappa < 6$. The one-dimensional form of the kappa distribution function can be obtained by integrating Eq. (1) over two velocity space coordinates as[17]

$$f_\kappa(v_s) = \frac{n_{0s}}{(\pi\kappa\theta_s^2)^{1/2}} \frac{\Gamma(\kappa)}{\Gamma(\kappa - 1/2)} \left[1 + \frac{v_s^2}{\kappa\theta^2}\right]^{-\kappa}. \quad (2)$$

Most of the plasma wave phenomena seen in the laboratory plasmas exist in space plasmas as well. However, detecting breaking of any wave in space plasmas is technologically difficult, because of the requirement of multiple spacecraft to track the evolution of the wave breaking process. Consequently, performing computer simulation is the best way to tackle such a problem in space plasmas. Recently, Kakad *et al.* performed the fluid[3,4] and particle-in-cell[21,22] simulations of the breaking of ion acoustic solitary waves (IASWs). They proposed that the long wavelength perturbation in the equilibrium electron and ion densities gives rise to two long-wavelength IASWs, which later breaks and evolves into multiple coherent solitary wave pulses. These pulses are like the solitons as they retain their shape during propagation in the system. They have shown that the initiation of the breaking of the wave depends on the amplitude and width of the perturbations, and on the plasma temperature.

Wave breaking is one of the components responsible for heating/acceleration of the charge particles in plasmas. As spacecraft observations show the presence of superthermal plasmas in the regions, where the particle acceleration processes are prominent, the simulations of the wave breaking process incorporating the superthermal population in the model are of great interest. Such simulation studies were not carried out in the past. In view of this, we perform a fluid simulation of the breaking of IASWs in the presence of superthermal electrons. The major achievement of this study is that we have been able to give a detailed understanding of the driving mechanism responsible for the wave breaking process in plasmas. The remaining flow of the paper is as follows: the plasma simulation model is discussed in Sec. II, the simulation results identifying initiation of the steepening and breaking in terms of various criteria are discussed in Sec. III, and in Sec. IV, we conclude the main results of the present study.

## II. PLASMA MODEL

We consider two-component unmagnetized collisionless plasma, which consists of cold ions and superthermal electrons.[23,24] The dynamics of ions is governed by the continuity and momentum equation as follows:

$$\frac{\partial n_i}{\partial t} + \frac{\partial (n_i v_i)}{\partial x} = 0, \quad (3)$$

$$\frac{\partial v_i}{\partial t} + v_i \frac{\partial v_i}{\partial x} = -\frac{q_i}{m_i} \frac{\partial \phi}{\partial x}, \quad (4)$$

where $n_i$ and $v_i$ are the density and velocity of the ions in the x-direction, respectively. $\phi$ is the electrostatic potential in the system, and $m_i$ and $q_i = +e$ are the mass and charge of the ions, respectively. In the model, superthermal electrons are regulated by the kappa velocity distribution function given by Eq. (2). The electron density is obtained by taking the first moment of the one-dimensional kappa velocity distribution function. It is written as

$$n_e = n_{e0} \left[1 + \frac{q_e\phi}{(\kappa - 3/2)k_BT_e}\right]^{-\kappa+1/2}. \quad (5)$$

In the equation above, $T_e$ is the temperature of the electrons and $q_e = -e$ is the electron charge. The electron and ion fluids are coupled by the Poisson equation

$$\frac{\partial^2 \phi}{\partial x^2} = -(q_i n_i + q_e n_e)/\epsilon_0. \quad (6)$$

At the equilibrium, plasma follows quasi-neutrality, under which the equilibrium ion density is equivalent to the equilibrium electron density, i.e., $n_{i0} = n_{e0}$. Here $n_{i0}$ and $n_{e0}$ are ion and electron density at the equilibrium. For simplicity, we normalized Eqs. (3)–(6) with appropriate scaling quantities. So, Eqs. (3), (4), and (6) can be written as

$$\frac{\partial N_i}{\partial t_n} + \frac{\partial (N_i U_i)}{\partial x_n} = 0, \quad (7)$$

$$\frac{\partial U_i}{\partial t_n} + U_i \frac{\partial U_i}{\partial x_n} = -\frac{\partial \Phi}{\partial x_n}, \quad (8)$$

$$N_e = \left(1 - \frac{\Phi}{\kappa - 3/2}\right)^{-\kappa+1/2}, \quad (9)$$

$$\frac{\partial^2 \Phi}{\partial x_n^2} = -N_i + N_e. \quad (10)$$

The ion fluid velocity $v_i$, the ion density $n_i$, the electron density $n_e$ and the electrostatic potential $\phi$ are normalized as $U_i = v_i/C_{IA}$, $N_i = n_i/n_{i0}$, $N_e = n_e/n_{e0}$, and $\Phi = e\phi/k_BT_e$, respectively. The space is normalized by the electron Debye length $\lambda_{De} = (k_BT_e\epsilon_0/n_{e0}e^2)^{1/2}$, and the time is normalized by inverse of the ion plasma oscillation frequency $\omega_{pi}^{-1} = (\epsilon_0 m_i/n_{i0}e^2)^{1/2}$. It gives $x_n = x/\lambda_{De}$, and $t_n = \omega_{pi}t$. The characteristic ion acoustic sound speed used in the velocity normalization is $C_{IA} = (k_BT_e/m_i)^{1/2}$.

In the fluid code, we solve Eqs. (7)–(10) numerically to obtain the electrostatic potential for different initial conditions and plasma parameters. The spatial derivatives in the model equations are computed numerically by using the fourth order finite difference method. We integrate equations in the time by using the leap-frog method with the time step $\Delta t$, which is second order accurate. The discretization in the space may generate the small wavelength numerical instability. Hence to

compensate that error, we use the fourth order compensating filter which has the expression as follows:[3,25]

$$F_h^* = \frac{5}{8}F_h + \frac{1}{4}(F_{h-1} + F_{h+1}) - \frac{1}{16}(F_{h-2} + F_{h+2}), \quad (11)$$

where $F_h$ represents physical quantity defined at grid point "$h$". This one-dimensional fluid simulation is performed over the periodic boundaries.

In the present simulation study, we assume that the flow velocity of the ion at $t = 0$ is zero, i.e., $v_i(x) = 0$. The equilibrium densities are set to be one, i.e., $n_{i0} = n_{e0} = 1$ and the initial electrostatic potential, $\phi = 0$. We perturbed these background densities by superimposing the Gaussian shape perturbation such that $n_s = n_{s0} + \delta n$. The form of the density perturbation is given as follows:[26,27]

$$n_s = n_{s0} + \Delta n \exp\left[-\left(\frac{x - x_c}{l_0}\right)^2\right]. \quad (12)$$

Here, $s = e, i$ for electrons and ions, respectively. In the equation above, $\Delta n$ is the amplitude of the perturbation, $n_{s0}$ is the equilibrium density of plasma species. $x_c$ is the center of the simulation system, and $l_0$ controls the width of the perturbation. We use the equal amplitude of perturbation in the density of the plasma species to satisfy the quasi-neutrality condition at $\omega_{pi}t = 0$. All simulation runs are performed for the grid spacing $\Delta x = 0.2\lambda_{De}$ and time interval $\omega_{pi}\Delta t = 0.1$. The system length, $L_x$ is considered as per the requirement to achieve stability before the pulse reaches to the boundaries of the system after breaking of the wave.

The algorithm of the fluid code works in the following fashion. We define the initial plasma parameters, such as the equilibrium density and velocity of each plasma species, the perturbation parameters ($l_0$ and $\Delta n$), and the value of the superthermal index, $\kappa$. We initiate the code with the identical perturbations in the equilibrium densities of the electrons and ions as defined by Eq. (12). By using the initial values of the variable $N_i$, $V_i$ and $\Phi$, the next time step values of $N_i$ and $U_i$ are obtained with the help of the time varying Eqs. (7) and (8). The main concern here is about the electron density, for which there is no time dependent equation to upgrade its value to the next time. We have Eq. (9) for the electron density, which is a function of the $\kappa$-index and $\Phi$. Hence, the electron density can be obtained for a given $\kappa$-index and the electrostatic potential at that time step. In this way, the $\kappa$-index is incorporated into the code through Eq. (9).

It may be noted that the electrostatic potential dependency of the electron density in Eq. (10) makes the Poisson solver numerically unstable with an implication of the method used by Kakad *et al.*[3,4,26,27] Hence, we use the iterative approach with the successive-over-relaxation (SOR) method for such a kind of Poisson equation.[23,28,29] The discretized form of the Poisson equation with the implication of the SOR method is as follows:

$$\bar{\Phi}_j^{r+1} = \Phi_j^r + \zeta\left[\Phi_j^{r+1} - \Phi_j^r\right] = (1 - \zeta)\Phi_j^r + \zeta\Phi_j^{r+1}. \quad (13)$$

Wherein the discretized equation of $\Phi_j^{r+1}$ is as follows:

$$\Phi_j^{r+1} = \frac{1}{2}\left\{\Phi_{j+1}^r + \Phi_{j-1}^{r+1} + \Delta x^2\left[N_i - \left(1 - \frac{\Phi^r}{k - 3/2}\right)^{-k+1/2}\right]_j\right\}. \quad (14)$$

In the equation above, $j$ is the grid point number, r is the iteration number which can be any integer, and $\zeta$ is the predefined constant which is known as the relaxation parameter. We considered $\zeta = 1.7$ for all our simulation runs. In the SOR method, the approximate value of the solution is improvised to $\bar{\Phi}_j^{r+1}$ by taking a weighted mean of $\Phi_j^r$ and $\Phi_j^{r+1}$, which are the previous and current iteration value of potential, respectively. To terminate these iterations, we have used following termination criteria in the simulation:

$$max|\Phi^r - \Phi^{r+1}| < \tau. \quad (15)$$

Here $\tau$ is tolerance. We have taken $\tau = 10^{-10}$ for all simulation runs. In solving the Poisson equation with the SOR method, initially, the value of $\phi$ at the previous time step is used as the initial guess. By using this guess value, the electron density calculated, which is substituted in Eq. (10), and then Eq. (10) is solved for the electrostatic potential. After every iteration, the newly calculated value of $\phi$ will be used for a new guess, and the procedure will be repeated. The iterations will stop after reaching the criteria given by Eq. (15). In this way, the kappa is incorporated in the calculation through Eq. (9). Due to the kappa density distribution the charge separation occurs, i.e., left-hand side of the Eq. (10) becomes finite. This charge separation leads to the generation of a finite electrostatic potential at the very first time step.

In order to observe the breaking phenomenon, selection of the width of the perturbation ($l_0$) is crucial in the simulation.[3] To discuss the role of $l_0$ in the wave breaking, we derive the linear dispersion relation of the IA waves from Eqs. (3)–(6) as[23]

$$\omega^2 = \frac{k^2\lambda_{De}^{*2}\omega_{pi}^2}{1 + k^2\lambda_{De}^{*2}}. \quad (16)$$

Here, $\lambda_{De}^* = \left(\frac{\kappa - 3/2}{\kappa - 1/2}\right)^{1/2}\lambda_{De}$ is the kappa dependent Debye screening length or modified Debye length. Equation (16) can be converged to the ion plasma frequency for $k^2\lambda_{De}^{*2} \gg 1$. This condition is possible only, when $k \gg \lambda_{De}^{*-1}$ i.e., when the wavelengths of the wave modes associated with the perturbation are less than the kappa dependent Debye screening length. This indicates that such a wave mode would contribute to the ion plasma oscillations, which are dispersive in nature. Furthermore, the wave modes with the wavelength greater than the kappa dependent screening length would contribute to the ion acoustic waves, which are nondispersive in nature.[30]

Generally, solitary waves are formed because of the balance between nonlinearity and dispersion in the plasma. Hence, in order to have stable solitary waves, the energy given to the system in the form of Initial Density Perturbation (IDP) should be distributed among all the dispersive as well as the nondispersive wave modes. However,

when the energy is given in the excess amount to only the nondispersive modes, then the system has to generate the dispersive modes to achieve the stability. This is achieved by disintegrating the long wavelength modes in the system into the short wavelength modes. This process is observed as the wave breaking in plasma. Hence, the condition $k \ll \lambda_{De}^{*-1}$ i.e., the wavelength of wave modes associated with the initial density perturbation should be greater than the kappa-dependent screening length of the system must be satisfied for the wave breaking phenomenon.

The power spectra obtained by taking the Fast Fourier Transform (FFT) of the perturbation helps us to identify the discretized power present in the different wavelengths associated with the perturbation. Figure 1 shows the power spectra of the two perturbations, which are obtained by taking the FFT of the perturbation as given by Eq. (12) for two different values of $l_0$, i.e., $l_0 = 20$ (red curve) and 30 (blue curve) by keeping fix $\Delta n$=0.4. Each of these power spectra gives the information of the power distributed over the wavelengths for two different perturbations. The two vertical lines in this plot indicate the wave numbers associated with the kappa dependent Debye screening length for $\kappa = 2$ and 20. These dash lines are used to identify the wavelengths greater (lesser) than the kappa-dependent screening length i.e., long (short) wavelength for specific kappa. Generally, wave numbers greater (lesser) than the dashed lines correspond to short (long) wavelengths. This is due to the inverse relationship of wave number with the wavelength. We observed that the increasing width of the perturbation restricted the power to the shorter k-range, which are associated with the long wavelength wave modes of the perturbation. Hence, breaking is expected for such values of $l_0$. We used this kind of initial perturbations in the present study.

We perform the fluid simulation for the different simulation parameters given in Table I. We consider 8 different values of the $\kappa$ index. For each value of the $\kappa$, amplitude of the perturbation is varied from 0.2–0.4 and then for each value of perturbation amplitude the width of perturbation is

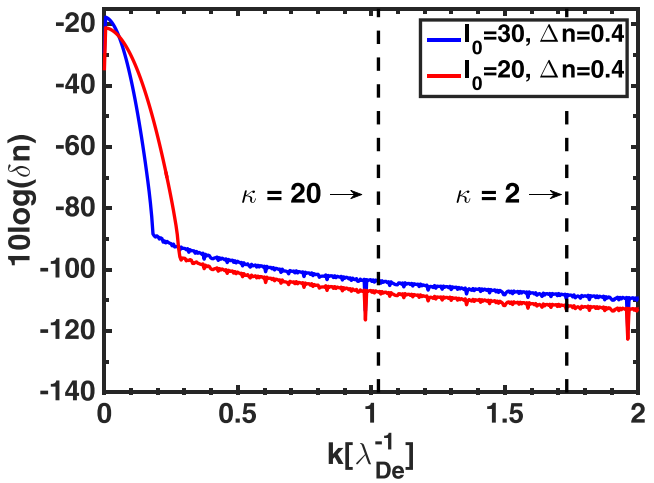


FIG. 1. The power spectra of the long-wavelength perturbation with $\Delta n = 0.4$ and $l_0 = 30$ and $\Delta n = 0.4$ and $l_0 = 20$. The two vertical lines in this plot indicate the wave numbers associated with the kappa dependent Debye screening length for $\kappa = 2$ and 20.

TABLE I. The input parameters used in the 200 simulation runs. We consider $\Delta x = 0.2\lambda_{De}$, $\Delta t = 0.1\omega_{pi}^{-1}$, and the system length $L_x = 20\,000\lambda_{De}$ for all simulation runs. The information of the specific simulation run is read as, e.g., Run-1(Ia). In this simulation run number, the number "1" specifies the $\kappa$ value, which is 2. The roman number I″ represents the perturbation amplitude i.e., 0.2 (20% of the equilibrium density), and the alphabet "a" is for the width value, which is 20. Hence, Run-5(IVe) has input $\kappa = 10$, $\Delta n = 0.35$, and $l_0 = 40$.

| | | Amplitude | | Width | |
|---|---|---|---|---|---|
| Run No. | $\kappa$ | Sub run No. | $\Delta n$ | Sub run No. | $l_0$ |
| 1 | 2 | | | | |
| 2 | 4 | I | 0.2 | a | 20 |
| 3 | 6 | II | 0.25 | b | 25 |
| 4 | 8 | III | 0.3 | c | 30 |
| 5 | 10 | IV | 0.35 | d | 35 |
| 6 | 13 | V | 0.4 | e | 40 |
| 7 | 17 | | | | |
| 8 | 20 | | | | |

varied from $20\lambda_{De}$–$40\lambda_{De}$. In this way, total 200 simulation runs are used in this study. These simulation run are used to get information on the onset of various stages in the wave breaking process. This analysis will help us to understand the role of different variables on the wave breaking process. Also, one of the runs from this table is used to explain the wave breaking process and the role of ponderomotive force on it in detail.

## III. SIMULATION RESULTS

### A. Generation of stable IASWs

First, we undertake the discussion of the various time stages involved in the generation of IASWs through the wave breaking process. Figure 2 shows the schematic of various stages up to and beyond the wave breaking of IASWs. We perturbed the system by using identical long-wavelength standard Gaussian perturbations in the ion and electron densities.[3] Due to the identical IDPs, the quasi-neutrality condition is satisfied, which gives zero electrostatic potential at $\omega_{pi}t = 0$. The electrons are in the nonthermal equilibrium, which creates charge separation in the system. The charge separation leads to the generation of finite electrostatic potential at the very first-time step i.e., $\omega_{pi}t = t_1$. The generated electrostatic potential at this stage is shown in Fig. 2(a). This electrostatic potential decreases with time. After falling to a certain amplitude threshold, the trough formation begins at the top of the potential pulse, which is shown in Fig. 2(b). The time corresponds to this stage (i.e., $\omega_{pi}t = t_2$) is termed as the "trough formation time". The trough at the center grows deeper with time. This leads to the formation of the two indistinguishable pulses at $\omega_{pi}t = t_3$ as depicted in Fig. 2(c). These pulses propagate opposite to each other towards the system boundaries. During propagation, their amplitude grows with time. After reaching a certain threshold, the trailing edges of both the pulses start to steepen. One of the snapshots of such pulses at time $\omega_{pi}t = t_4$ is shown in Fig. 2(d). The time corresponding to the initiation of the steepening, we termed it as "steepening time". At the maximum

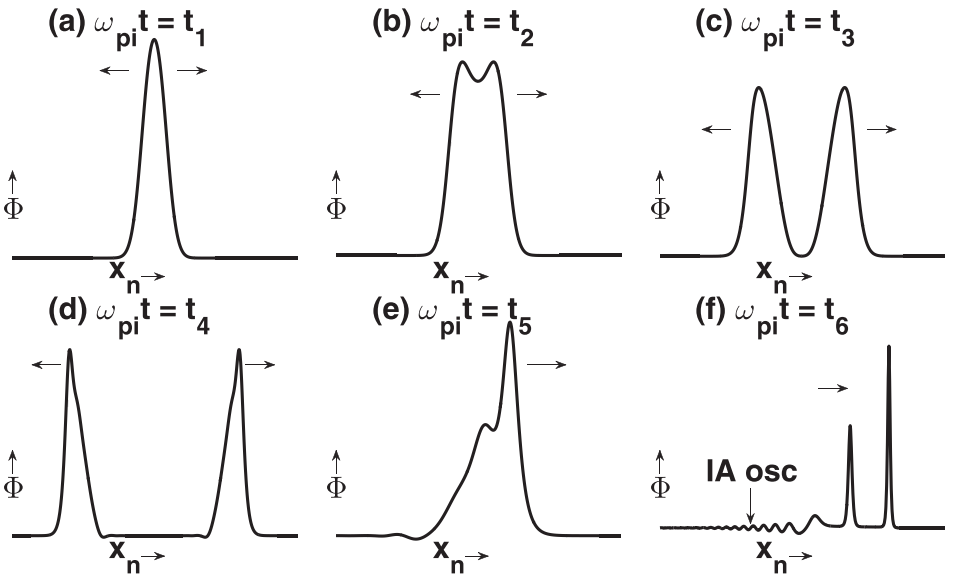


FIG. 2. Schematic of the evolutionary stages of the electrostatic potential involved in the generation of a chain of stable IASWs through the wave breaking process. IA oscillations (IA osc) following the chain of stable IA solitons are marked in panel (f).

steepening, the amplitude of the pulses reaches a critical amplitude after which the IASW pulses break. One of the schematics closed to the initiation of the wave breaking is shown in $\omega_{pi}t = t_5$ in Fig. 2(e). The time step at which the initiation of the breaking starts is referred to as the "wave breaking time". The breaking of both pulses leads to the formation of two chains containing two or more coherent IASW pulses. Subsequently, on the trailing edge of the smallest pulse, small amplitude oscillations are formed. These are ion acoustic oscillations. The ion acoustic oscillations generally move with speed $v_{s0}$, which is less than the speed of any solitary wave pulse in the chains. Each of the solitary pulses in the chain propagates with a different speed. It is observed that the solitary pulse amplitude is directly proportional to the pulse velocity. Hence, after some time, these pulses and IA oscillations are well separated from each other. This leads to the stable propagation of the IASW pulses after some time. A schematic of the chain of stable IASW pulses along with IA oscillations propagating towards the right-side of the simulation boundary at $\omega_{pi}t = t_5$ is shown in Fig. 2(f).

### B. Spatio-temporal evolution of coherent IASWs

To get more insights into the evolution and propagation of the IASW structures in strongly (smaller $\kappa$) and weakly (larger $\kappa$) nonthermal plasmas, we examine the spatial and temporal evolution of the IASWs in two simulation runs. Figure 3 shows the spatio-temporal evolution of the electrostatic potential ($\phi$) for (a) Run-1(Vc) ($l_0 = 30$, $\Delta n = 0.4$ with $\kappa = 2$) and (b) Run-8(Vc) ($l_0 = 30$, $\Delta n = 0.4$ with $\kappa = 20$). We used $20\,000\lambda_{De}$ as the system length for both simulation runs, however, for the better visualization the spatial window in the figure is restricted as per the requirement. Here, $x - x_c = 0$ represents the center of the system. The inset plot in each panel of Fig. 3 shows a zoomed portion of

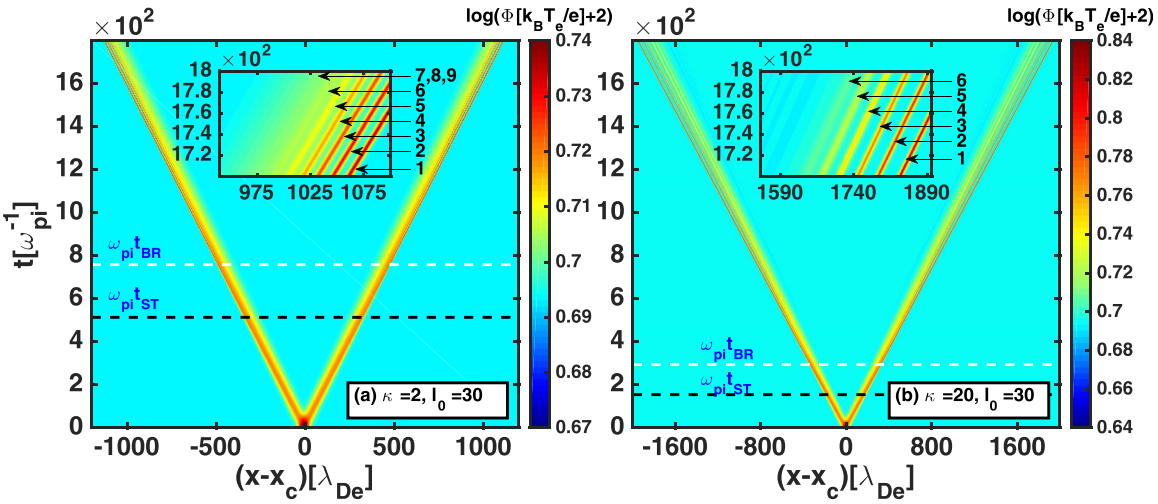


FIG. 3. The spatial and temporal evolution of the electrostatic potential in the system for the case Run-1(Vc) ($l_0 = 30$, $\Delta n = 0.4$, $\kappa = 2$), and Run-8(Vc) ($l_0 = 30$, $\Delta n = 0.4$, $\kappa = 20$). The inset shows the zoomed portion of the right side propagating pulses. In this, the dark red and yellow bands correspond to the IASW pulses, whereas the alternate dark and light blue bands are due to the IA oscillations. The black and white horizontal dashed lines indicate the steepening ($\omega_{pi}t_{ST}$) and breaking ($\omega_{pi}t_{BR}$) time of the wave, respectively. The numbers represent the IASW pulse number in the chain. It may be noted that in panel-(a), the pulses 7, 8, and 9 are not yet evolved to form distinct solitary pulses. Hence, they are shown by just a single arrow. At the final stage, 9 and 6 number of solitons are formed in Run-1(Vc) and Run-8(Vc), respectively.

the main figure for better visualization of the separated IASW pulses and IA oscillations. The red and yellow color bands in these insets are due to the evolving IASW pulses, whereas the alternate dark and light blue bands represent the IA oscillations. In both runs, there are two sets of red and yellow bands, which represent the presence of two sets of evolving IASW pulses. One group propagates toward the right side boundary, whereas the other propagates toward the left side boundary. The inverse of the slope of these color bands gives the phase velocity of the respective pulses. The pulses propagating toward the right side boundary has positive slopes, whereas those propagating toward the left-side boundary have negative slopes. This is due to one chain of pulses moving in the opposite direction of the other. In Fig. 3(a), the slope of the red and yellow bands is higher than the slope of the red and yellow bands in Fig. 3(b). This indicates that the IASW pulses have smaller propagation speed in plasma with higher superthermal population (i.e., $\kappa = 2$) in comparison with the plasma with lower superthermal population (i.e., $\kappa = 20$). In Figs. 3(a) and 3(b), the horizontal dashed black lines are drawn at the steepening time, and the white lines are drawn at the wave breaking time. The criteria adopted to identify steepening and wave breaking time of IA pulses are discussed in Subsection III E. From Fig. 3, we observed that the steepening and breaking occur early for the system with the less superthermal population (larger $\kappa$). The time interval between the steepening and breaking of the wave is also found less for such a plasma system. The amplitude of the IASWs found to be smaller in the system with a more superthermal population (i.e., $\kappa = 2$) than the system with a less superthermal population (i.e., $\kappa = 20$). However, the number of pulses formed after breaking of the long wavelength IA pulse are more (i.e., 9) in the highly superthermal populated system than the lower superthermally populated system (i.e., 6).

### C. Dispersion characteristics before and beyond wave breaking

In general, the free energy given to the system in the form of the IDP gets transferred to the different wave modes in the system. From the dispersion characteristics of the evolving system, we can understand the existing wave modes and their strength at different stages of the evolution. We obtain the $\omega - k$ diagram by taking the Fast Fourier Transformation (FFT) of the electrostatic potential in space and time. Figure 4 shows the dispersion diagram of Run-1(Vc) ($l_0 = 30, \Delta n = 0.4$ with $\kappa = 2$) and Run-8(Vc) ($l_0 = 30, \Delta n = 0.4$ with $\kappa = 20$) during two phases, namely before, and after wave breaking. In these plots, the grey and white dashed lines, respectively, represents the linear dispersion relation obtained with ($N_i = N_e$) and without ($N_i \neq N_e$) the plasma approximation.[23] Figure 4(a) is the dispersion diagram of the Run-1(Vc) for the time $\omega_{pi}t = 0 - 178$, which is for the time up to which the formation of two pulses takes place, i.e., before the breaking time. In this figure, we can see that the energy given in form of the IDP is transferred to the long-wavelength modes; hence the maximum power is restricted to the shorter $k$ range. A similar dispersion trend is observed for the Run-8(Vc) during the time $\omega_{pi}t = 0 - 109.2$, (i.e., before breaking time) except the power distributed among the $k$ range, which is more for $\kappa = 20$ than $\kappa = 2$. To understand the distribution of free energy in the modes after wave breaking, we plot FFT after breaking of the wave. Figures 4(c) and 4(d) are the respective FFTs of the Run-1(Vc) for the time $\omega_{pi}t = 900 - 1078$ and Run-8(Vc) for the time $\omega_{pi}t = 600 - 709.2$. The dispersion characteristics show that the energy which was restricted to the shorter $k$ range before wave breaking is now shared among the large $k$ range. This indicates that the breaking of the wave generates shorter wavelength modes in the system, and thus induces the dispersive effects in the plasma system.

### D. Evolution of the energies during the generation of stable IASWs

We compute the maximum kinetic energy of ions $(KE)_{imax} = \frac{1}{2}(U_i^2)_{max}$, and the maximum electrostatic potential energy $Es_{max} = \frac{1}{2}(E^2)_{max}$ in the simulation runs. As an

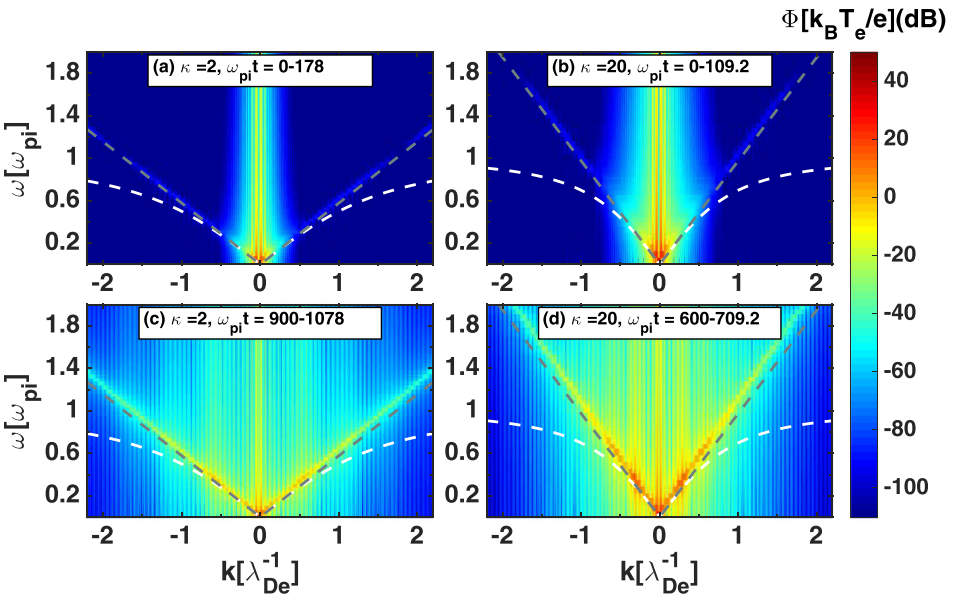


FIG. 4. $\omega$-$k$ dispersion diagram for before and after wave breaking time for the Run-1(Vc) and Run-8(Vc). The upper (lower) two panels show FFT before (after) wave breaking.

example, the evolution of the $Es_{max}$ and $(KE)_{imax}$ for the Run-1(Vc) and Run-8(Vc) is shown in Fig. 5. The dashed vertical lines in this figure indicate the timing of the different evolutionary stages that we have discussed in Fig. 2. The evolution of $(KE)_{imax}$ for Run-1(Vc) and Run-8(Vc) is demonstrated in Fig. 5(a). In this figure, the red curve is for the run with $k = 20$, and the blue curve is for the run with $\kappa = 2$. For the both cases, we observe the similar trend of the evolution of the kinetic energy. The $(KE)_{imax}$ is initially zero because there are no ion motions, and then it gradually increases with the increase of the finite electrostatic potential in the system and achieves first maxima at the trough formation time, $t_2$. After the trough formation, $(KE)_{imax}$ further remains constant for a long time, and then it starts to increase again with the initiation of the IA pulse steepening. This increase in the $(KE)_{imax}$ continues until the IA pulses become stable. After achieving the stability by the IA pulses, the $(KE)_{imax}$ observed was almost constant. In Fig. 5(b), the time evolution of the maximum of electrostatic potential energy $Es_{max}$ is depicted. At the very first time step, the finite potential is generated in the system, hence $Es_{max}$ starts with the finite value. The $Es_{max}$ remains constant until the wave steepening, and thereafter it starts increasing. This increase in the $Es_{max}$ is continued until the stability of the pulses. The $Es_{max}$ remains almost constant after achieving the stability by these pulses.

### E. Wave speed and ion acceleration during steepening and wave breaking

To understand the effects of the wave breaking on the ion fluid, and IASW propagation velocity ($V_p$), we plotted the variation of the phase velocity of the waves and maximum ion fluid velocity. Figure 6(a) demonstrates the phase velocity of the IASW pulse in the high and low superthermal population systems. We calculate the phase velocity after the trough formation time, as the wave propagates only after the trough formation. We can see that the phase velocity reaches the finite value after some time of the trough formation. The $V_p$ remains approximately constant until the formation of the two long-wavelength IASW pulses. The phase velocity increases thereafter, and it reaches the maximum. We consider this particular time as the time of the steepening of the

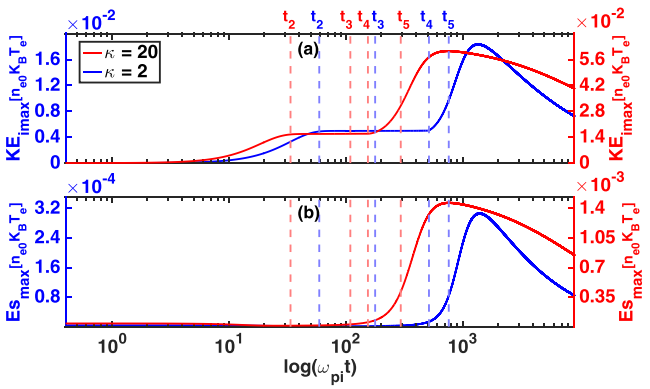


FIG. 5. Time evolution of the (a) the maximum kinetic energy of the ions ($KE_{imax}$), and (b) maximum electrostatic potential energy ($Es_{max}$) in the system for Run-1(Vc) and Run-8(Vc).

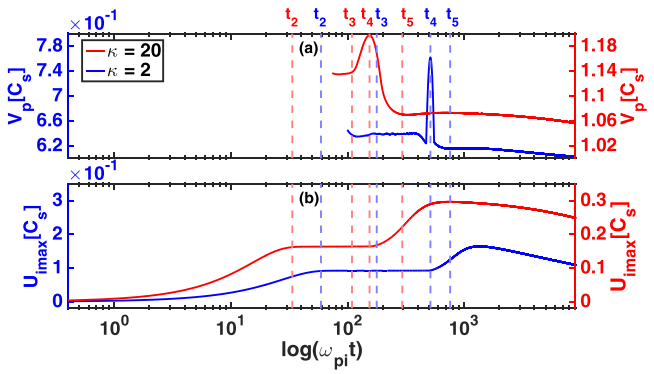


FIG. 6. The time variation of the (a) maximum phase velocity ($V_p$) of the IASW pulse and (b) maximum ion fluid velocity ($U_{imax}$) for Run-1(Vc) and Run-8(Vc).

IA pulse (i.e., $\omega_{pi}t_{ST}$). Later it decreases, and this decrease continues until the breaking of the IA pulse. As the pulse break, $V_p$ slightly increases thereafter. It should be noted that, after wave breaking, the maximum phase velocity is calculated for the leading pulse in the chain. The phase velocity of each pulse in the chain becomes almost constant after achieving the stability.

In Fig. 6(a), we observed that the magnitude of phase speed (Vp) is smaller for small kappa index as compared to the large kappa. This is identical to the results obtained from the nonlinear fluid theory by Saini *et al.*[24] and the fluid simulation by Lotekar *et al.*[23] This kappa dependence can be explained on the basis of understanding given by Hapgood *et al.*[31] and Kourakis *et al.*[19] As mentioned in Sec. II, the kappa dependent screening Debye length $(\lambda^*_{De})$ is a function of kappa index, and it decreases with a decrease in the kappa value. This happens because when we decrease the $\kappa$-index by keeping mean energy constant in the particle velocity distribution, there will be an increase in the lower and higher energy electron population and a decrease in the middle energy electron population.[31,32] The Debye length of the plasma system is defined by the energy of major population in the system. Since for smaller (larger) kappa, major population in the system is low (middle) energy population, so the Debye length is shorter (longer). In this case, the ion acoustic speed $(C_{IA})$ in superthermal plasma changes to the modified ion acoustic speed $(C^*_{IA})$, which is defined as

$$C^*_{IA} = \omega_{pi}\lambda^*_{De} = C_{IA}\left(\frac{\kappa - 3/2}{\kappa - 1/2}\right)^{1/2}. \tag{17}$$

This manifests that the ion acoustic speed decreases with the decreasing of the kappa index. Hence, our observation of the decreasing phase speed of the wave with the decreasing kappa index in the simulation is justified.

Figure 6(b) shows a variation of the maximum of ion fluid velocity for Run-1(Vc) and Run-8(Vc). The ion fluid responds to the growing perturbation in plasma. Hence, $U_{imax}$ gradually increases with time. At the time of the formation of the trough, the $U_{imax}$ reaches its first local peak. There after $U_{imax}$ remains constant until the steepening time. After the steepening time, the $U_{imax}$ starts to increase again. This increase in $U_{imax}$ stops after the formation of the stable

IASW pulses. The trends of $V_p$ and $U_{imax}$ profile are observed to be same for the system with $\kappa = 2$ and $\kappa = 20$, except their magnitudes.

### F. Ponderomotive force in the course of evolution of the stable IASWs

Ponderomotive force is a nonlinear force that a charged particle experienced in an inhomogeneous oscillating electric field. In our plasma model, the dynamical ions experience this force when they are in an inhomogeneous oscillating electric field. The ponderomotive force acting on the ion fluid is given by the following expression:

$$F_p = -\frac{1}{4}\frac{e^2}{m_i\Omega_p^2}\frac{\partial}{\partial x}|E|^2. \tag{18}$$

In the equation above, $\Omega_p$ is the oscillating frequency of the electric field. The above equation can be rewritten for the ponderomotive frequency $\Omega_p$ as follows:

$$\Omega_p^2 = \frac{1}{4}\frac{Es}{KE_i}\omega_{pi}^2, \tag{19}$$

where $KE_i$ and $Es$ are the ion kinetic and electrostatic energy, and $\omega_{pi}$ is the ion plasma frequency. By using the normalization used in Sec. II, Eqs. (18) and (19) can be written as

$$F_{pn} = -\frac{1}{4}\frac{1}{\Omega_{pn}^2}\frac{\partial}{\partial x_n}|E_n|^2, \tag{20}$$

$$\Omega_{pn}^2 = \frac{1}{4}\frac{Es}{KE_i}. \tag{21}$$

In the equation above, the ponderomotive force ($F_{pn}$) is normalized by the factor $(k_BT_e/\lambda_{De})$, whereas the ponderomotive frequency ($\Omega_{pn}$) is normalized with the ion plasma frequency ($\omega_{pi}$). Here, the normalized ponderomotive potential is given by

$$\Psi_{pn} = \frac{1}{4}\frac{1}{\Omega_{pn}^2}|E_n|^2. \tag{22}$$

Recently, Kakad *et al.*[4] have studied the variation of the ponderomotive frequency and the ponderomotive potential in the course of wave breaking of IASWs. We have performed a similar kind of exercise for the superthermal plasma. The time variation of the normalized ponderomotive maximum potential (panel-a), the ponderomotive frequency (panel-b), and the maximum ponderomotive force (panel-c) for Run-1(Vc) and Run-8(Vc) is given in Fig. 7. The vertical blue (red) dashed lines in this figure indicate the time of the various stages of the breaking process for Run-1(Vc) [Run-8(Vc)] as discussed in the schematics shown in Fig. 2. In Fig. 7(a), we can see that the ponderomotive potential gradually increases with time, and has the first peak at the time of the trough formation. This indicates either increase in the electric field amplitude or decrease in the ponderomotive frequency as per Eq. (21). In both the simulation runs, we observe that the amplitude of the potential pulse decreases (i.e., the initial amplitude of the electric field decreases),

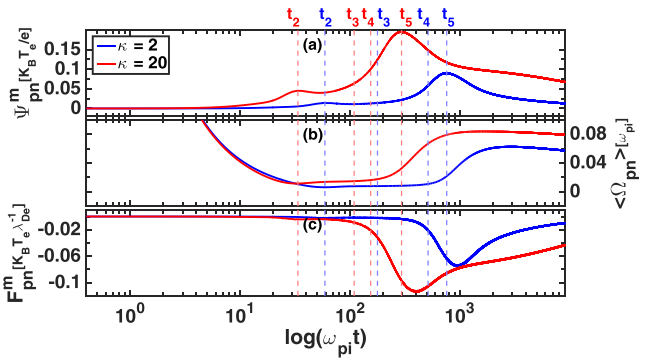


FIG. 7. The evolution of the (a) maximum ponderomotive potential ($\psi_{pn}^m$), (b) average ponderomotive frequency ($\langle\Omega_{pn}\rangle$), and (c) the maximum ponderomotive force ($F_{pn}^m$) for Run-1(Vc) and Run-8(Vc).

initially. During this time, the ponderomotive frequency also decreases with time. We understood from this that the increase in the $\Psi_{pn}$ is due to the decrease in the $\Omega_{pn}$. The initially given perturbations in the electron and ion densities setup the finite electric field that drives the IA waves in the simulation. The ions are effectively accelerated by the field of IA waves during its propagation as seen in Fig. 6. This resulted in increasing kinetic energy of the ions. At the same time, the potential energy decreases due to decrease of the electrostatic potential. The increasing kinetic energy of the ions and the decreasing potential energy reduce the ponderomotive frequency, which ultimately enhances the ponderomotive potential, and attains the peak at the trough formation time, $\omega_{pi}t = t_2$. After time $t_2$, the $\Psi_{pn}$ starts decreasing due to increase of the $\Omega_{pn}$. However, this decrease in the $\Psi_{pn}$ does not sustain for a long time. The $\Psi_{pn}$ started increasing gradually again at the time somewhere around $t_3$, i.e., the time at which the formation of two long-wavelength IA pulses occurred. The ponderomotive potential grows faster after $t_3$, and then attains again maxima at the time of breaking of the long-wavelength IASW pulses. This increase of ponderomotive force is due to the steepening (around $t_4$) that leads to an increase in the amplitude of the long-wavelength IA pulse. The electric field associated with the IA wave is the maximum at the breaking time ($t_5$). Therefore, the ponderomotive potential has peaked at the wave breaking time. After breaking of the IA pulse, the ponderomotive potential decreases. The amplitude of the broken IASW pulse increases ahead of its breaking. However, instead of growing, the ponderomotive potential decreases. This is due to the increase of ponderomotive frequency at the wave breaking that leads to the decrease in the ponderomotive potential. This decrease of the ponderomotive potential continues until the formation of the chains of stable IASW wave structures. The ponderomotive potential remains almost constant after the IASW pulses attain stability. This is due to the constant amplitude of the stable pulses in the chain. It should be noted here that, after breaking, we considered the amplitude of the leading (faster) pulse as the maximum amplitude in the system. In this way, we can use the maxima of the ponderomotive potential as proxies to identify the trough formation and initiation of the wave breaking in the system.

Now the main question arises from our simulation study is that how the ponderomotive force drives the breaking of the long-wavelength IA pulse. To address this, we obtain the variation of ponderomotive force over the space for each time step for the simulation Run-8(Vc) ($l_0 = 30, \Delta n = 0.4$ with $\kappa = 20$). The evolution of electrostatic potential along with the spatially varying magnitude of the ponderomotive force on it is shown in the multimedia Fig. 8 (Multimedia view). The snapshots at various stages during the evolution of the stable IASW structures are shown in this figure. The arrows in this figure show the direction, and its length represents the magnitude of the ponderomotive force acting on the ion fluid. The length of the directional arrows is normalized by the maximum ponderomotive force amplitude present at that time. The red color arrows indicate the direction of the force towards the right side, and the green arrows indicate its direction towards the left side. Figure 8(a) (Multimedia view) shows the finite potential pulse generated after introducing the perturbation in the system. During this stage, we can see that the ponderomotive pull on the ion fluid does not balance. Especially, the pull on the bottom-side of the pulse is magnitude wise greater than the top side of the pulse. Hence, bottom-side ion fluid pulled apart due to these left and right side forces, which reduces the ion fluid density at the center of the pulse. As a result, the amplitude of the pulse decreases with the increase in the pulse width. This change in the shape of the potential pulse decreases the ponderomotive force magnitude. In the panel (b), we can see the decrease in the ion fluid density at the centre due to the spreading of the fluid at the bottom of the pulse. In Fig. 8(b) (Multimedia view), the amount of fluid dispersed by the top side ponderomotive force towards the right is almost equal to the fluid dispersed by the right top side ponderomotive force. Due to the bottom side opposite pull of the ponderomotive force, the fluid density at the center further decreases which leads to the formation of two indistinguishable pulse forms. The two indistinguishable pulses along with the magnitude and direction of the ponderomotive force on the pulses are shown in Fig. 8(c) (Multimedia view). Since these pulses are identical, it is expected that the dynamical behavior of the ponderomotive force on each of this pulse will be the same. Therefore, among these two pulses, we further show the dynamical behavior of the ponderomotive force on the pulse that propagates to the right-side boundary of the system. In Fig. 8(d) (Multimedia view), we can see that the top side ponderomotive force pushes the ion fluid toward the left side, whereas, the bottom side force pulls the fluid towards the right side. Due to this configuration of the force, the ion fluid starts dispersing toward the trailing edge of the pulse that increases the ion density over there. This increase in the ion density changes the electrostatic potential due to which the trailing edge of the potential pulse is stretched, which is depicted in Fig. 8(d) (Multimedia view). The leftward ponderomotive force continues to disperse the ion fluid on the left side, due to which the pulse trailing edge spreads. As a result of the transportation of the fluid, the density just

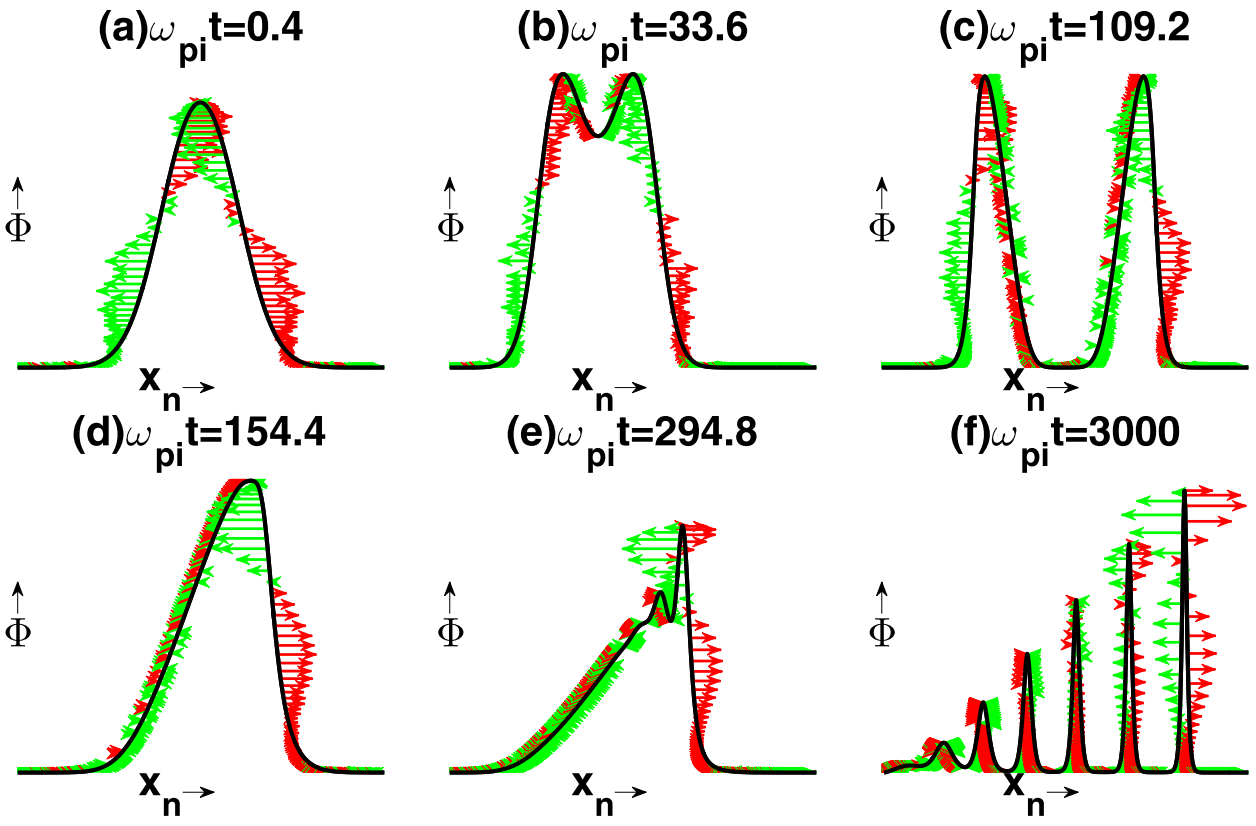


FIG. 8. The static figure shows snapshots of the electrostatic potential at various time steps of the evolution of stable IASW structures. The magnitude and direction of the spatially varying ponderomotive force acting at different locations on the shape of evolving potential pulse are shown with the arrows. A detailed animation of the variation of magnitudes of the ponderomotive force during the evolution of stable IASW structures is illustrated in the multimedia version of this figure. Multimedia view: https://doi.org/10.1063/1.4991467.1

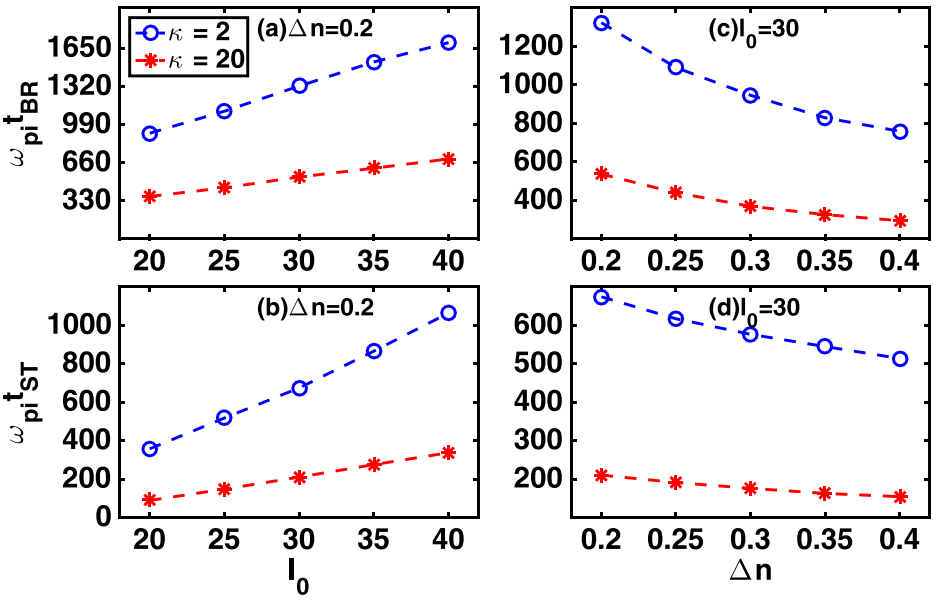


FIG. 9. The variation of the breaking and steepening time with respect to the perturbation width ($l_0$), and the perturbation amplitude ($\Delta n$) for the runs discussed in Table I.

beside the left side of the maximum potential decreases. This leads to the initiation of the wave breaking, which is presented in Fig. 8(e) (Multimedia view). As the breaking initialized, the rightward pull of the ponderomotive force on the top side fluid (shown on the right side of the potential by the red arrows) starts becoming stronger. This force then helps to sustain the Gaussian-like shape of the pulse as it will try to conserve the fluid in that region by pushing it back, which is drifted by the leftward ponderomotive force. Hence, wave breaking continues until the formation of the perfect Gaussian shaped pulse. This process leads to the formation of the stable solitary pulses that moves with constant speed and amplitude. One of the snapshots of this stage is shown in Fig. 8(f) (Multimedia view). In this figure, we can see the perfect balance between the ponderomotive force on the left and right side of the pulses. The animation of the evolution of stable IASW pulses along with the dynamical behaviour of the ponderomotive force acting spatially on it is given in the multimedia file.

### G. Effects of perturbation and superthermal population on the onset of steepening and breaking of the long wavelength IASW

To understand the effects of the width and amplitude of the IDP on the steepening and breaking of IASWs, we perform simulations for various combinations of $\Delta n$ and $l_0$ for small ($\kappa = 2$) and large ($\kappa = 20$) values of $\kappa$. We plotted variation of the breaking time (panel-a) and steepening time (panel-b) with respect to the width of the Gaussian perturbation for fix $\Delta n = 0.2$ in Fig. 9. From panels (a) and (b), we understand that the breaking and steepening time increases with increase in the width of the perturbation. Figures 9(c) and 9(d), respectively, illustrate the variations of the breaking and steepening times with the amplitude of the perturbation at a constant width, $l_0 = 30$. These figures demonstrate that the breaking and steepening time decreases with increasing perturbation amplitude. To understand the effects of the superthermal populations on the onset time of the breaking and steepening, we plot the breaking and steepening time for the different $\kappa$ for the same perturbation parameters, i.e., $\Delta n = 0.4$ and $l_0 = 30$. This is shown in Fig. 10. We conclude from this figure that the increase of the superthermal population (i.e., decrease of $\kappa$) delays the onset of the steepening and breaking of the IASW in superthermal plasmas.

## IV. DISCUSSION AND CONCLUSIONS

In this paper, we perform the fluid simulation to understand the dynamics of the wave breaking of IASWs in superthermal plasmas. We identified the time of onset of steepening and wave breaking for IASW by using some standard proxies, and then studied their dependence on the kappa index ($\kappa$), which limits the superthermal population in the plasma system. Our simulation demonstrates that the excess superthermal population in the plasma delays the steepening and breaking of the long-wavelength IASWs.

The perturbation in the equilibrium electron and ion densities creates a small charge separation that drives the generation of positive amplitude IA structures. This positive potential sets up the bipolar electric field. Due to the gradient

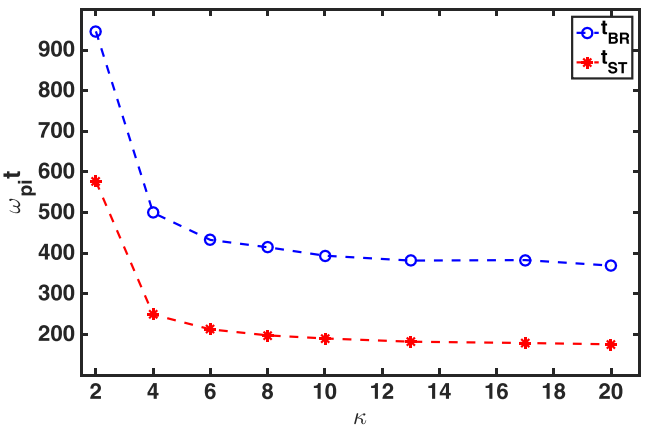


FIG. 10. Breaking and steepening time of the long-wavelength IASW as a function of the superthermal index. For this profile, we consider the fixed perturbation form with $l_0 = 30$ and $\Delta n = 40$ in all simulation runs.

of the electric field, the ponderomotive force acts differently on the ion fluid. This ponderomotive force drives the ion fluid towards the system boundaries. The magnitude of the ponderomotive force is higher for $\kappa = 20$ than $\kappa = 2$. Furthermore, the amplitude and phase velocity of the IASW pulses in the plasma with $\kappa = 20$ is higher than $\kappa = 2$. The superthermal population has a prominent effect on the ion acceleration. The smaller superthermal electron population favours more ion fluid acceleration than the plasma with the larger superthermal population.

It is seen that the wave breaking transfers energy to the shorter wavelength modes. This energy transfer happens due to the imbalanced ponderomotive force during the propagation of the long-wavelength IASWs. We have seen that the ponderomotive force is not balanced before the wave breaking. The $F_{pn}$ acts more on the front side of the pulse than the trailing side. Whenever the oscillating ion fluid comes to this region, the amplitude of the fluid oscillation altered by the $F_{pn}$ in such a way that the wavelength of fluid oscillation decreases. In this way, short-wavelength modes are generated in the system. As the $F_{pn}$ on both sides of the pulse perfectly balances, the generation of the short-wavelength stops, and they will not be spread in a larger $k$ range after that.

The increase in the phase velocity of the long-wavelength IA pulse after their generation can be used as a proxy to identify the steepening of the IA wave. In other words, it indicates the acceleration of IASWs before the initiation of wave steepening. The increase of the ion fluid speed at the breaking of the wave indicates that the wave breaking process accelerates the ion fluid. We have observed that the acceleration depends on the superthermal population. The wave breaking in the weakly superthermal plasma system (i.e., with $\kappa = 20$) accelerates ions more as compared to the breaking in the highly superthermal populated system (with $\kappa = 2$).

Our simulation confirms the maximum ponderomotive potential at the onset of breaking of the long-wavelength IASWs. This is identical to that of Kakad and Kakad,[4] who proposed this criterion as one of the proxies to identify breaking of the IASWs. The ponderomotive potential reaches the maximum due to the growing amplitude of the pulse that reaches to the wave breaking amplitude threshold because of the steepening of the trailing side of the pulse. Since, the ponderomotive potential is directly proportional to the square of the electric field amplitude, the ponderomotive potential increases with the increase of the electric field.

From the ponderomotive force analysis, we conclude that the $F_{pn}$ plays an essential role in the formation of the stable IASW pulses. For the formation of the stable IASWs, $F_{pn}$ needs to be in balance like shown in Fig. 8(f) (multimedia view). The breaking of the long-wavelength IASW pulse continues until the perfect balance of the ponderomotive force on each side of the newly formed short wave length IASW pulse in the chain.

In conclusion, our simulation demonstrates that the initial density perturbation, the superthermal population, and the pondermotive force on the plasma species play an important role in the initiation of the steepening and breaking of the IASWs. This study may be useful in explaining the chain of solitary wave structures observed in the space plasma regions where the superthermal plasma exists.

## ACKNOWLEDGMENTS

The model computations were performed on the High Performance Computing System at the Indian Institute of Geomagnetism.

[1]J. M. Dawson, Phys. Rev. **113**, 383 (1959).
[2]R. Davidson and P. Schram, Nucl. Fusion **8**, 183 (1968).
[3]A. Kakad, Y. Omura, and B. Kakad, Phys. Plasmas **20**, 062103 (2013).
[4]A. Kakad and B. Kakad, Phys. Plasmas **23**, 122101 (2016).
[5]S. Bame, J. Asbridge, H. Felthauser, E. Hones, and I. Strong, J. Geophys. Res. **72**, 113–129, https://doi.org/10.1029/JZ072i001p00113 (1967).
[6]S. Christon, Icarus **71**, 448–471 (1987).
[7]C. Kletzing, J. Scudder, E. Dors, and C. Curto, J. Geophys. Res.: Space Phys. **108**(A10), 1360, https://doi.org/10.1029/2002JA009678 (2003).
[8]V. Formisano, P. Hedgecock, G. Moreno, F. Palmiotto, and J. Chao, J. Geophys. Res. **78**, 3731–3744, https://doi.org/10.1029/JA078i019p03731 (1973).
[9]V. Pierrard and J. Lemaire, Radiat. Measure. **26**, 333–337 (1996).
[10]F. Xiao, C. Shen, Y. Wang, H. Zheng, and S. Wang, J. Geophys. Res.: Space Phys. **113**, A05203, https://doi.org/10.1029/2007JA012903 (2008).
[11]G. Gloeckler, J. Geiss, H. Balsiger, P. Bedini, J. Cain, J. Fischer, L. Fisk, A. Galvin, F. Gliem, D. Hamilton *et al.*, Astron. Astrophys. Suppl. Ser. **92**, 267–289 (1992), available at http://adsabs.harvard.edu/full/1992A%26AS...92..267G.
[12]M. Maksimovic, V. Pierrard, and P. Riley, Geophys. Res. Lett. **24**, 1151–1154, https://doi.org/10.1029/97GL00992 (1997).
[13]H. Ikezi, R. Taylor, and D. Baker, Phys. Rev. Lett. **25**, 11 (1970).
[14]Y. Nakamura and A. Sarma, Phys. Plasmas **8**, 3921–3926 (2001).
[15]S. Olbert, *Physics of the Magnetosphere* (Springer, 1968), pp. 641–659.
[16]V. M. Vasyliunas, J. Geophys. Res. **73**, 2839–2884, https://doi.org/10.1029/JA073i009p02839 (1968).
[17]D. Summers and R. M. Thorne, Phys. Fluids B: Plasma Phys. **3**, 1835–1847 (1991).
[18]M. Hellberg, R. Mace, T. Baluku, I. Kourakis, and N. Saini, Phys. Plasmas **16**, 094701 (2009).
[19]I. Kourakis, S. Sultana, and M. Hellberg, Plasma Phys. Controlled Fusion **54**, 124001 (2012).
[20]V. Pierrard and M. Lazar, Sol. Phys. **267**, 153–174 (2010).
[21]A. Kakad, B. Kakad, and Y. Omura, Phys. Plasmas **24**, 060704 (2017).
[22]B. Kakad, A. Kakad, and Y. Omura, Phys. Plasmas **24**, 102122 (2017).
[23]A. Lotekar, A. Kakad, and B. Kakad, Phys. Plasmas **23**, 102108 (2016).
[24]N. Saini, I. Kourakis, and M. Hellberg, Phys. Plasmas **16**, 062903 (2009).
[25]Y. Omura and J. L. Green, J. Geophys. Res.: Space Phys. **98**, 9189–9199, https://doi.org/10.1029/92JA02901 (1993).
[26]B. Kakad, A. Kakad, and Y. Omura, J. Geophys. Res.: Space Phys. **119**, 5589–5599, https://doi.org/10.1002/2014JA019798 (2014).
[27]A. Kakad, B. Kakad, C. Anekallu, G. Lakhina, Y. Omura, and A. Fazakerley, J. Geophys. Res.: Space Phys. **121**, 4452–4465, https://doi.org/10.1002/2016JA022365 (2016).
[28]A. Kakad, A. Lotekar, and B. Kakad, Phys. Plasmas **23**, 110702 (2016).
[29]A. Lotekar, A. Kakad, and B. Kakad, "An effective approach to implement the Maxwellian and nonMaxwellian distributions in the fluid simulation of solitary waves in plasmas," (unpublished).
[30]C. Uberoi, *Introduction to Unmagnetized Plasmas* (PHI Learning Pvt. Ltd., 1997).
[31]M. Hapgood, C. Perry, J. Davies, and M. Denton, Planet. Space Sci. **59**, 618–629 (2011).
[32]D. Bryant, J. Plasma Phys. **56**, 87–93 (1996).